Original citation:
Marshall, Kenneth, Walker, Marc, Walton, Richard I. and Hatton, Ross A.. (2016) Enhanced stability and efficiency in hole-transport-layer-free CsSnI3 perovskite photovoltaics. Nature Energy, 1. 16178.

Enhanced Stability and Efficiency in Hole-Transport Layer Free $CsSnI_3$ Perovskite Photovoltaics

K. P. Marshall[1], M. Walker[2], R. I. Walton[1], and R. A. Hatton[1]*

[1]Department of Chemistry, University of Warwick, CV4 7AL, UK.

[2]Department of Physics, University of Warwick, CV4 7AL, UK.

*ross.hatton@warwick.ac.uk

Abstract

Photovoltaics based on tin halide perovskites have not yet benefitted from the same intensive research effort that has propelled lead perovskite photovoltaics to >20% power conversion efficiency, due to the susceptibility of tin perovskites to oxidation, the low energy of defect formation and the difficultly in forming pin-hole free films. Here we report $CsSnI_3$ perovskite photovoltaic devices without a hole-selective interfacial layer that exhibit a stability ~10 times greater than devices with the same architecture using methylammonium lead iodide perovskite, and the highest efficiency to date for a $CsSnI_3$ photovoltaic: 3.56%. The latter results in large part from a high device fill-factor, achieved using a strategy that removes the need for an electron blocking layer or an additional processing step to minimise the pinhole density in the perovskite film, based on co-depositing the perovskite precursors with $SnCl_2$. These two findings raise the prospect that this class of lead-free perovskite photovoltaic may yet prove viable for applications.

Introduction

Lead-free perovskite photovoltaics (PPVs) using tin halide as the light harvesting semiconductor have not yet benefitted from the same intensive research effort that has propelled lead PPVs from a power conversion efficiency (η) of ~3.8% in 2009[1] to >20% today[2], because of the susceptibility of tin to oxidation from the 2+ to the 4+ oxidation states upon exposure to air, a transformation that does not occur easily in lead perovskites.[3,4] Consequently, the record η for tin halide PPVs lags behind that of lead PPVs at ~6%, achieved using $CH_3NH_3SnI_3$ sandwiched between a mesoporous TiO_2 hole-blocking layer (HBL) and doped spiro-OMeTAD electron blocking layer (EBL).[5,6] The low energy of formation of tin array vacancies in tin halide perovskites has also proved problematic, making it difficult to achieve high device fill-factor (*FF)* due to high rates of defect mediated charge carrier recombination.[7,8] Similar to the case of lead perovskites, a further challenge has been in achieving solution processed thin films of tin perovskites with a low density of pin-hole defects, to avoid undermining device *FF*.[9] Beyond being lead-free, tin halide perovskites offer a number of properties which make them attractive for use in PPVs provided the challenge with stability can be addressed, including narrower band gaps than their lead analogues (1.3-1.4 eV)[10,11], low exciton binding energies (~18 meV)[12,13] and high charge mobilities[11,14,15].

To date reports relating to the use of tin halide perovskites as the light harvester in PPV devices[5,6,8,9,16–21] are relatively few in number, and the η has primarily been limited by a sub-optimal *FF*.[5,6,8] Kumar *et al.*[8] have shown that PPVs based on $CsSnI_3$ sandwiched between a TiO_2 HBL and triphenylamine EBL (*FF* ~ 0.3) are stable when stored under nitrogen, although the stability in air and/or under continuous illumination was not reported. Hao *et al*.[6] have shown that after 24 hours under nitrogen the η of devices based on $CH_3NH_3SnI_3$ sandwiched between a TiO_2 HBL and spiro-OMeTAD EBL (*FF* ~ 0.48) was reduced by 64%, even with encapsulation. Similarly, Noel *et al.*[5] reported that PPVs based on $CH_3NH_3SnI_3$ with the same charge selective interlayers (*FF* ~ 0.5) degrade within minutes when tested under ambient conditions, and Zhang *et al.*[21] have reported that unencapsulated PPV devices based on $HC(NH_2)_2SnI_2Br$, using PEDOT:PSS and $PC_{61}BM$ charge extraction layers, failed within minutes of exposure to air.

Recently we have shown how the efficiency of PPV devices based on the black polymorph of $CsSnI_3$ perovskite; (B)-γ $CsSnI_3$, sandwiched between a fullerene HBL and copper iodide EBL, can be improved by incorporating an excess of SnI_2 into the $CsSnI_3$ film[19] - The B-γ phase is of most relevance for photovoltaic applications because it exists below 89°C.[11] Unfortunately, the stability of those devices was relatively poor with a ≥ 30% loss in η when stored in the dark in ambient air for 1 hour.[19] Herein we have extended this investigation to explore the potential of SnF_2, $SnCl_2$ and $SnBr_2$ additives in $CsSnI_3$ based PPVs, which has yielded some important new findings that enable the device fabrication process and architecture to be simplified, whilst simultaneously greatly increasing η. We show that $SnCl_2$ stands out as being a particularly beneficial additive, and that simplifying device architecture by removing the EBL dramatically improves device stability. Crucially, removal of the EBL layer does not reduce device η when $SnCl_2$ additive is co-deposited with the $CsSnI_3$ layer.

Probing B-γ $CsSnI_3$ film structure and stability

It is known that B-γ $CsSnI_3$ degrades to the zero-dimensional Sn(IV) salt Cs_2SnI_6 in ambient air and that the absorption coefficient of Cs_2SnI_6 in the visible spectrum is a factor of 10 times smaller than that of B-γ $CsSnI_3$.[14] Consequently, it is possible to monitor the oxidation of thin films of $CsSnI_3$ in air by measuring the evolution of the electronic absorption spectrum with time, as shown in Figures 1a and 1b.

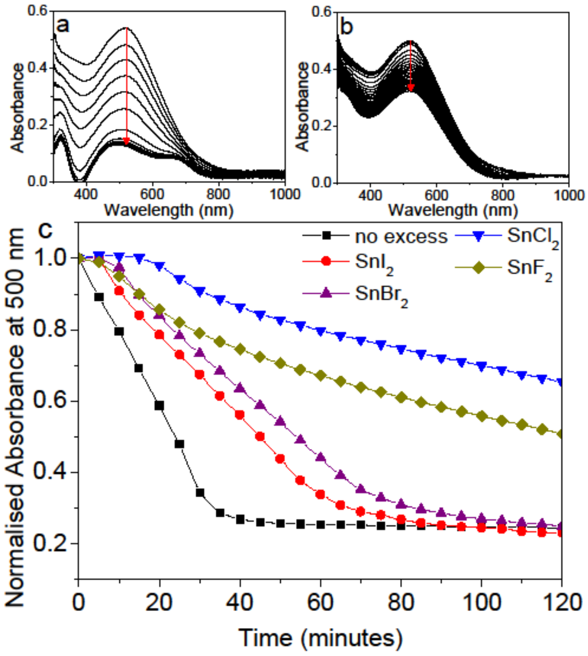

Figure 1 | Evolution of the absorption spectrum of $CsSnI_3$ films with different tin halide additives in ambient air. **a** $CsSnI_3$; **b** $CsSnI_3$ + 10% $SnCl_2$; and **c** normalised absorbance at 500 nm for $CsSnI_3$ with 10 mol% of SnI_2, $SnBr_2$, $SnCl_2$ or SnF_2, and with no tin halide additive. In all cases the $CsSnI_3$ solution concentration was 8 wt% which resulted in a film thickness of ~50 nm. All films supported on indium tin oxide (ITO) coated glass. The red vertical lines indicate the direction of change with increasing time in ambient air. [See Supplementary Discussion]

It is evident from Figure 1c that of the four tin halides investigated $SnCl_2$ results in the highest film stability. Based on the time taken for the absorbance at 500 nm to reduce by 30%, films with $SnCl_2$ are more stable by a factor of ~3.7 times as compared to $CsSnI_3$ films with 10 mol% excess SnI_2, and a factor of ~6.7 times compared to films with no tin halide additive. The scanning electron microscope (SEM) images in Figure 2 show that the former cannot be attributed to a difference in film porosity because films prepared with 10 mol%

$SnCl_2$ have a comparable or higher pin-hole density to films prepared with 10 mol% excess SnI_2, $SnBr_2$ or SnF_2.

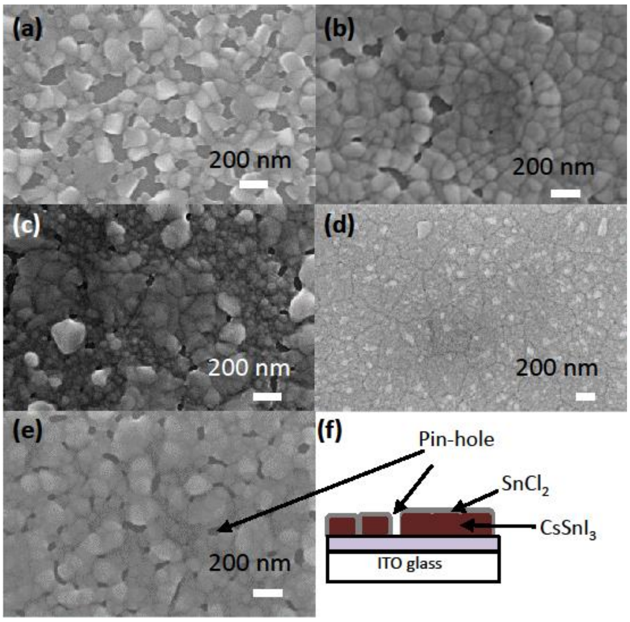

Figure 2 | SEM images of $CsSnI_3$ films on ITO glass prepared with different tin halide additives. **a** no tin halide additive, **b** 10 mol% added SnI_2, **c** 10 mol% added $SnBr_2$, **d** 10 mol% added SnF_2, **e** 10 mol% added $SnCl_2$. **f** Schematic diagram of proposed film structure in case (e): $CsSnI_3$ crystallites capped with a thin $SnCl_2$ layer (see later discussion for the justification of this model).

Corroborating evidence for the large improvement in $CsSnI_3$ film stability when prepared with 10 mol% $SnCl_2$ is provided by the evolution of the X-ray diffraction (XRD) pattern of thin films with time exposed to ambient air; Figure 3 and Supplementary Figure 1.[11,22] Figure 3a shows how the intensity of one of the most intense reflections; the (202) Bragg peak, in the B-γ $CsSnI_3$ diffraction pattern, disappears completely with time, and so this peak serves as a good probe for monitoring the oxidation of B-γ $CsSnI_3$ to Cs_2SnI_6 in air. It is evident from a comparison of Figures 3a & 3d that addition of $SnCl_2$ dramatically improves film stability, since after 3 hours of air exposure this peak has ~80% of its starting intensity, whilst it has almost completely disappeared for the $CsSnI_3$ film prepared with no tin halide additive.

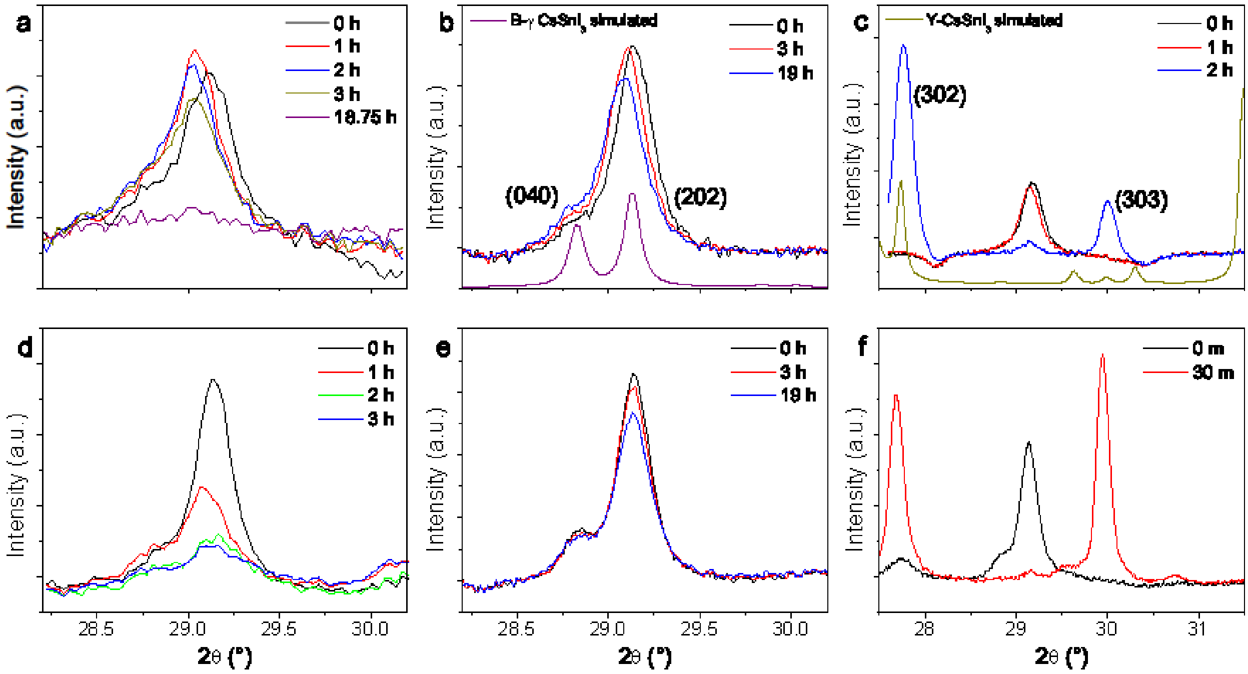

Figure 3 | Evolution of XRD patterns of $CsSnI_3$ films with and without $SnCl_2$ additive under different conditions. XRD patterns of thin films of $CsSnI_3$ prepared with 10 mol% $SnCl_2$ additive with exposure to; **a** 25% humid air, **b** dry air, and **c** humid nitrogen. XRD patterns of thin films of $CsSnI_3$ exposed to **d** 25% humid air, **e** dry air, and **f** humid nitrogen.

It is evident from Figures 3b and 3e that B-γ $CsSnI_3$ is stable in dry air, but converts to the yellow phase (Y-$CsSnI_3$) in a humid nitrogen atmosphere (Figure 3c and 3f). It is therefore only with the combined action of water and oxygen that Cs_2SnI_6 is formed, which is in agreement with a study of bulk samples reported by Stoumpos *et al.*[15] Notably, Cs_2SnI_6 is a narrow band gap semiconductor with a high electron and hole mobility,[14,23,24] properties that are very different from those of the decomposition products of lead perovskites.

High resolution X-ray photoelectron spectroscopy (HRXPS) analysis reveals that there is only one Cl 2p environment in $CsSnI_3$ films prepared with 10 mol% $SnCl_2$ which has the same binding energy as for $SnCl_2$ (Figure 4), consistent with the Cl not being incorporated into the perovskite structure. This suggests that the $SnCl_2$ is present as a thin film or layer of particles at the perovskite crystallite surfaces as schematically illustrated in Figure 2f. To confirm this hypothesis we have measured the atomic percentage of the different elements that make up the surface of a compact film of $CsSnI_3$ with 10 mol% $SnCl_2$ (Supplementary Figure 2) and a thickness of ~ 80 nm, using HRXPS for angles of X-ray incidence of 90° and 30°. Reducing the incident angle halves the sampling depth from ~ 8 nm to ~ 4 nm. For an angle of incidence of 90° the Cl percentage composition is 36.4% (Supplementary Table 1), which is several times higher than would be expected if Cl was evenly distributed throughout the thickness of the film. For an angle of incidence of 30° the Cl percentage increases to 42.9%, while the I percentage decreases from 18.8% to 15.3% and the Cs percentage decreases from 21.9% to 18.1%, compelling evidence that the $SnCl_2$ is concentrated at the surface of the $CsSnI_3$ crystallites. Further direct evidence for this conclusion is provided by argon ion sputtering the film surface (Supplementary Figure 3), since the atomic percentage Cl decreases rapidly as the surface is etched, whilst the I concentration increases and then saturates. The conclusion that Cl is not incorporated into the $CsSnI_3$ lattice is also consistent with the observation that solid solutions of $CsSnI_{3-x}Cl_x$ are not formed from stoichiometric DMF solutions of the halide precursors.[25] The latter likely stems from the large difference in ionic radii between Cl and I (1.81 Å for Cl and 2.2 Å for I),[26] and/ or the very different structures of $CsSnCl_3$ and $CsSnI_3$ at room temperature, which are monoclinic and orthorhombic respectively.[25] Additionally Peedikakkandy *et al.*[25] have shown that a processing temperature of 70 °C is needed to form $CsSnCl_3$ from DMF solutions, which may explain why we do not find evidence for the presence of the $CsSnCl_3$ perovskite when processing at room temperature. When films of $SnCl_2$ alone or $CsSnI_3$ with 10 mol% $SnCl_2$ are exposed to ambient air for one hour the Cl 2p peaks in both spectra shift to higher binding energies by the same amount (Figure 4a - lower & 4b - lower), and the intensities of the two weak O1s peaks at 530.7 eV and 532.1 eV (Supplementary Figure

4(b)), assigned to SnO_2[27] and H_2O, respectively, is increased by ~10-fold. The insight as to the differing roles of water and oxygen provided by the XRD patterns, together with the changes in the XPS spectra upon exposure to air, are consistent with the $SnCl_2$ surface layer functioning as a desiccant which sacrificially oxidises slowing the oxidation of the underlying $CsSnI_3$ by H_2O, since $SnCl_2$ is known to form a stable hydrate ($SnCl_2{\cdot}2H_2O$) as well as oxidising to form SnO_2.[28]

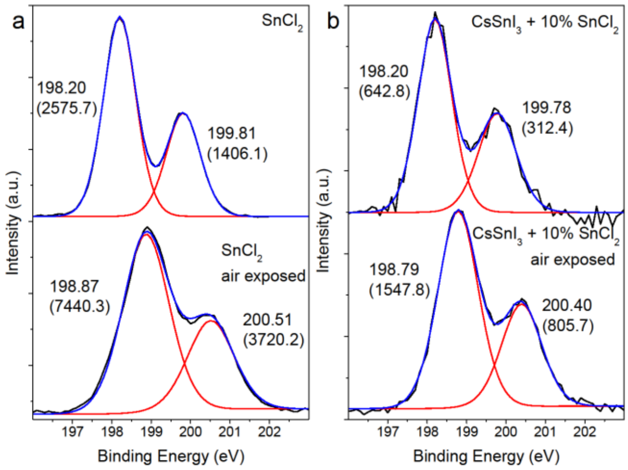

Figure 4 | HRXPS Cl 2p spectra of films of $SnCl_2$ and $CsSnI_3$ + 10 mol% $SnCl_2$ before and after exposure to ambient air. **a** $SnCl_2$ with and without 1 hour of air exposure; **b** $CsSnI_3$ + 10 mol% $SnCl_2$ with and without 1 hour of air exposure. The measured spectra, peak deconvolution and the sum of the fitted peaks are given by black, red and blue lines respectively. Fitting performed using CasaXPS software (see Methods Section). Peak positions and intensities labelled on figures.

Photovoltaic device studies

To test if the improvement in film stability towards air exposure translates into improved stability in PPVs, devices with a simplified architecture were fabricated, based on a planar heterojunction using $PC_{61}BM$ as the HBL and $CsSnI_3$ as the light harvesting layer. This structure simplifies device fabrication and reduces the number of parallel degradation pathways that can complicate the interpretation of device stability studies. A simplified architecture is also attractive from a commercial perspective, since fabrication costs typically increase with increasing number of processing steps.[29] Of the four additives; $SnCl_2$, SnI_2, $SnBr_2$ and SnF_2, PPV devices using $SnBr_2$ and SnF_2 exhibited poor device performance with $\eta \leq 0.4\%$ (Supplementary Table 2) and/or poor device yield and so were not investigated further. Initially $SnCl_2$ loadings of 5, 10 and 15 mol% were investigated (Supplementary Figure 5 and Supplementary Table 3), and a loading of 10 mol% was found to give the highest yield of working devices combined with a narrow photocurrent spread. Consequently 10 mol% tin halide is the additive loading used in all studies hereafter described. Importantly, the current-voltage characteristics of devices recorded in forward and reverse sweep for a range of starting voltages and scan rates exhibit no significant hysteresis (Supplementary Figure 6).

Immediately after fabrication, devices with a $SnCl_2$ additive are 60-70% more efficient than those using SnI_2 and a factor of 4 times more efficient than without tin halide additive, due to higher J_{sc}, V_{oc} and FF; Supplementary Table 4. Importantly, when stored under nitrogen (< 5 ppm O_2 and < 1 ppm H_2O) there are further large improvements in the η of devices with tin halide additives, on the time scale of weeks to several months (Figures 5a&b (Supplementary Table 4) & 5c&d (Supplementary Table 5)). Indeed, the onset of significant improvements begins after only 1 week with ~10% improvement in V_{oc} and FF (Supplementary Figure 7(a)), although there is no change in either the electronic absorption spectrum or X-ray diffraction pattern of the perovskite film (Supplementary Figure 7(b)&(c)). Notably this additional improvement is particularly pronounced for devices that have a low shunt resistance when tested immediately after fabrication, as shown in Figures 5c&d (Supplementary Table 5).

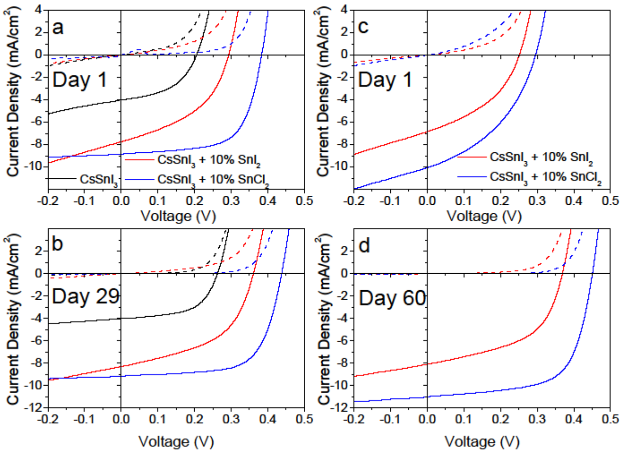

Figure 5 | Current-voltage (*JV*) characteristics of $CsSnI_3$ PPVs before and after a period of extended storage under nitrogen. Representative *JV* characteristics for devices with the structure: ITO|$CsSnI_3$|$PC_{61}BM$|BCP|Al using $CsSnI_3$ with 10 mol% $SnCl_2$, 10 mol% SnI_2 and with no additive as the light harvesting layer and $PC_{61}BM$ as the HBL. Devices were tested immediately after fabrication (a and c) and after storage under nitrogen for an extended period (b and d).

To our knowledge the *FF* is the highest achieved for a tin halide PPV; mean value of 0.63 and champion value of 0.69, which is particularly impressive given that there is no EBL and the perovskite film has a high density of pinholes (Figure 2e). Furthermore, whilst $CsSnI_3$ films with 10 mol% $SnCl_2$ prepared from 8 wt% solution have a much greater density of pinholes than those prepared from 16 wt% solution (Supplementary Figure 8), the device *FF* is improved (Supplementary Figure 9 and Supplementary Table 6), consistent with the $SnCl_2$ preventing electrons moving from the $PC_{61}BM$ into the ITO electrode.

The simplest possible explanation for the improved device performance with $SnCl_2$ additive is that the $SnCl_2$ forms a > 1 nm thick hole-selective layer at the ITO|$CsSnI_3$ interface. However, ultra-violet photoelectron spectroscopy (UPS) measurements

(Supplementary Figure 10 a&b) show that the valence band of $SnCl_2$ is 6.6 ± 0.1 eV below the vacuum level, which is well below that measured for $CsSnI_3$ at 4.9 eV ± 0.1 eV (Supplementary Figure 11), in close agreement with that reported by Chung *et al.*[30] . Consequently, a $SnCl_2$ layer at this interface with a thickness > 1 nm would be expected to impede rather than facilitate hole-extraction, thereby degrading device *FF* - which is not observed. Alternatively, it is possible that a layer of $SnCl_2$ with a thickness ≤ 1 nm is buried at the ITO|$CsSnI_3$ interface which, whilst sufficiently thin to be transparent to the flow of charge carriers, could perturb the interfacial energetics by modifying the surface potential at the ITO electrode. To explore this possibility, measurements of the work function of the ITO electrode were made using a Kelvin probe before and after deposition of $SnCl_2$ from a DMF solution having the same $SnCl_2$ loading as used to achieve 10 mol% $SnCl_2$ in a 8 wt% $CsSnI_3$ solution: 2.4 mg ml^{-1} $SnCl_2$. The work function of ITO treated with DMF only was measured to be 4.76 ± 0.06 eV. Following treated with 2.4 mg ml^{-1} $SnCl_2$ solution the work function is essentially unchanged at 4.72 eV ± 0.08 eV, which is a strong indication that the energetics for hole-extraction are neither improved nor degraded when $SnCl_2$ is added to the $CsSnI_3$ layer at the loading used.

A more likely explanation for the improvement in device performance is that the excess $SnCl_2$ at the surface of the $CsSnI_3$ crystallites moderately *n*-dopes the fullerene layer, forming a Schottky barrier to the unwanted extraction of electrons from the fullerene into the ITO electrode at the site of pinholes in the perovskite film, thereby allowing the devices to function well without the need for a EBL. The dark current-voltage characteristics re-plotted on a log-linear scale (Supplementary Figure 12) validate this conclusion, since the current in reverse bias is dramatically reduced with the $SnCl_2$ additive; by ~10 times at a bias of – 1 V. This interpretation requires that the $SnCl_2$ at least partially diffuses into the fullerene layer and that there is an electron donating interaction from the $SnCl_2$ to the fullerene, giving rise to an *n*-type doping effect. To confirm this hypothesis UPS measurements were performed on a ~40 nm thick $PC_{61}BM$ film spin cast onto a gold substrate pre-coated with a very thin (<

3 nm) film of $SnCl_2$. The results of these measurements are summarised in Figure 6, from which it is evident that the energy difference between the Fermi level (E_f) and valence band (HOMO) edge increases by 240 meV when $SnCl_2$ is at the buried interface, consistent with *n*-type doping. It is not possible to determine the dopant density very close to the interface and at the site of the pinholes in the $CsSnI_3$ film, although if the coverage of $SnCl_2$ over the surface of the $CsSnI_3$ crystallites is approximately even - as schematically depicted in Figure 2f - then the $SnCl_2$ dopant density will be highest at the site of the pinholes in the perovskite film.

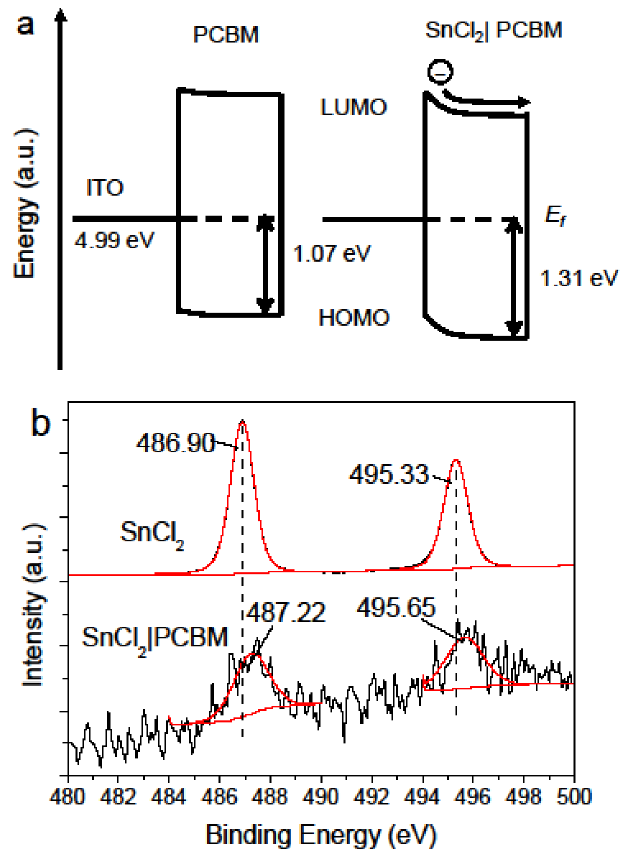

Figure 6 | Band diagrams depicting the energy level alignment at the ITO | $PC_{61}BM$ interface and spectroscopic evidence for an *n*-type doping interaction. **a** Energy level diagram of an ITO| $PC_{61}BM$ interface with and without $SnCl_2$ derived from the UPS data given in Supplementary Figure 10. The energy of the highest occupied molecular orbital (HOMO) and lowest unoccupied molecular orbital (LUMO) for $PC_{61}BM$ are depicted. The measured difference between the HOMO and Fermi level (E_f) in the $PC_{61}BM$ with and without $SnCl_2$ doping: 1.31 eV and 1.07 eV respectively. **b** HRXPS spectra of the Sn 3d region from a thin film of $SnCl_2$ (labelled $SnCl_2$) and a film of $PC_{61}BM$ doped with $SnCl_2$ (labelled SnCl2|$PC_{61}BM$). The red lines correspond to curve fitting performed with CasaXPS (See Methods Section) and the vertical dashed grey lines are to guide the eye.

Consequently, the barrier to hole-extraction from the fullerene layer at the site of pinholes is likely to be considerably larger. Corroborating evidence for *n*-type doping is provided by HRXPS of the same films (Figure 6b), which shows that the binding energy of the Sn 3d orbitals in $SnCl_2$ is increased by 0.4-0.5 eV when incorporated in a $PC_{61}BM$ film, consistent with partial electron transfer from the $SnCl_2$ to the $PC_{61}BM$. Based on a bandgap of 1.3 eV[11,15,25] the energy of the conduction band edge of $CsSnI_3$ is 3.6 eV below the vacuum level, which is considerably shallower in energy than the LUMO of $PC_{61}BM$ at 3.78 eV[31] below the vacuum level, and so there is unlikely to be a barrier to electron extraction across this interface either with or without $SnCl_2$ doping of the $PC_{61}BM$ layer.

Figure 7 shows the performance of $CsSnI_3$ PPV devices without encapsulation and tested in ambient air at a humidity of ~25% under constant 1 sun simulated solar illumination. After 45 minutes continuous illumination the device temperature stabilised at ~ 50 °C. To our knowledge the stability of these devices is the highest reported for any tin halide PPV to date: On average, η reduces to 70% of its starting value only after ~7 hours under continuous 1 sun illumination in ambient air, with the best performing devices taking 16 hours to reduce to the same value (Figure 7a)). The improvement in stability reported herein is a factor of 20 greater than devices with the same architecture fabricated using $CH_3NH_3PbI_{3-x}Cl_x$ in place of $CsSnI_3$ fabricated in our laboratory, and 10-fold more stable than reported independently by the group of Zhang *et al.*[29], also for the same device architecture

(Figure 7a). Crucially this exceptional stability for a tin-perovskite PV is common to devices with and without metal halide additive, consistent with the dispersing of the $SnCl_2$ into the PCBM layer, and so is tentatively attributed to the removal of the EBL. However, champion stability is exhibited only by devices with a tin halide additive: 11 hours with no additive; 16 hours with 10 mol% $SnCl_2$; and 22 hours for SnI_2. Crucially using $SnCl_2$ as an additive offers the advantage of the highest η, due to reduced sensitivity of device parameters to pin-holes, without complicating the process of device fabrication.

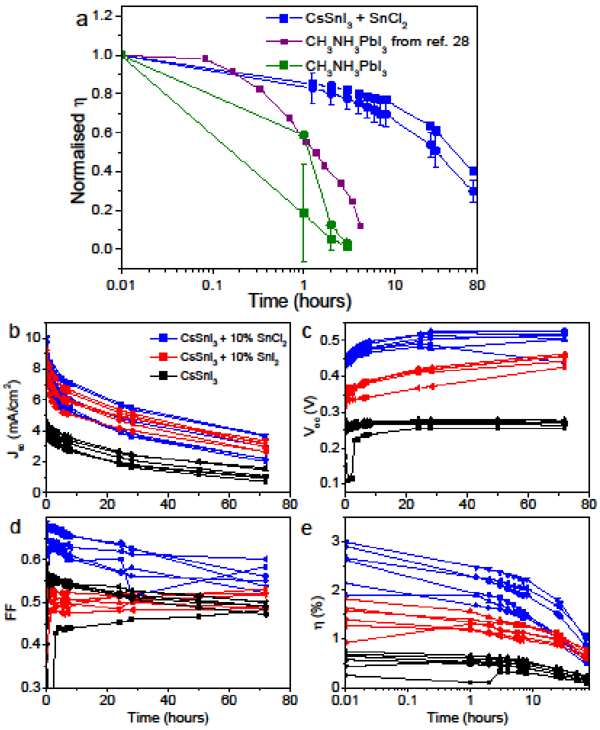

Figure 7 | PPV device stability tests under 1 sun constant illumination in ambient air for unencapsulated devices with the same architecture. **a |** Mean (squares) and champion (circles) normalised η for PPV devices *without encapsulation* tested in ambient air under continuous 1 sun simulated solar irradiation with the structure: (blue) ITO | $CsSnI_3$ + 10 mol% $SnCl_2$ | $PC_{61}BM$ | BCP | Al at ~ 25% humidity and ~50 °C.; (green) ITO | $CH_3NH_3PbI_3$ | $PC_{61}BM$ |BCP | Al at ~ 25% humidity and ~50 °C.; (purple) ITO | $CH_3NH_3PbI_3$ | $PC_{61}BM$ |Bis-

C_{60} | Ag reported in Ref. 29. Error bars are ± 1 standard deviation. A linear-linear plot of this data is also given in Supplementary Figure 13. **b-e |** Evolution of *JV* characteristics for a representative set of unencapsulated devices tested in air under continuous 1 sun simulated. The devices have the structure: ITO glass / $CsSnI_3$ + X / $PC_{61}BM$ / BCP / Al, where X = 10 mol% $SnCl_2$ (blue), 10 mol% SnI_2 (red) or no additive (black). The temperature under the lamp stabilised at ~ 50 °C after 45 minutes continuous illumination. All curves are guides to the eye.

It is evident from Figure 7 (b-e) that most of the degradation in device η is due to loss in J_{sc}, whilst *FF* is very stable and V_{oc} actually increasing by ~10% for all devices. The increase in V_{oc} can be attributed to the improved crystallisation in the fullerene layer that occurs when the device is subject to intense light for an extended period, which reduces the number of LUMO tail states that erode V_{oc}[32,33] and/or partial oxidation of the electrode to form a very thin low work function aluminium oxide layer. The good stability in device *FF* indicates that the series resistance in these devices does not change significantly as the light harvesting ability deteriorates. This observation is consistent with the fact that Cs_2SnI_6 is a weak absorber of light and has a high electron mobility[23,34], and is compelling evidence that the barriers to electron transport across the $CsSnI_3$ / Cs_2SnI_6 and Cs_2SnI_6 / $PC_{61}BM$ are small. That is, the Cs_2SnI_6 layer that forms at the $CsSnI_3$/fullerene interface as a result of air oxidation allows electron transport, whilst not significantly contributing to light harvesting.

The fact that devices with and without $SnCl_2$ have nearly comparable stability, in conjunction with evidence for *n*-type doping of the fullerene layer, indicates that in devices the $SnCl_2$ is no longer confined at the $CsSnI_3$ surface but is dispersed in the adjacent fullerene layer. Further evidence for this, and for a significant interaction between $SnCl_2$ and $PC_{61}BM$, is provided by the electronic absorption spectra shown in Supplementary Figure 14, which shows how the absorbance of a ~ 50 nm thick $CsSnI_3$ film prepared with 10 mol%

$SnCl_2$ at a wavelength of 450 nm changes with time exposed to ambient air, with and without a $PC_{61}BM$ overlayer. It is evident that the $CsSnI_3$ with 10 mol% added $SnCl_2$ becomes less stable when buried beneath a layer of $PC_{61}BM$ which is consistent with partial removal of the $SnCl_2$ from the perovskite surface. Conversely, Supplementary Figure 14b shows that washing with chlorobenzene has no detrimental effect on the perovskite film stability, which together is compelling evidence for a strong interaction between $PC_{61}BM$ and $SnCl_2$. Notably, whilst the Al electrode is evidently able to slow the ingress of water and oxygen into the device sufficiently for a stability study on the time scale reported herein - consistent with lifetime studies of organic PV devices using a very similar HBL[35] – its long term barrier properties are limited.[35] It is anticipated that further significant improvements in device stability can be achieved by using an electron extracting electrode with better barrier properties towards ambient water and oxygen.

Discussion

Taken together the aforementioned experiments provide compelling evidence that $SnCl_2$ is the best of the tin halides investigated for the current application. The reason for this is almost certainly a complex interplay between a number of factors including the following: (i) Firstly, Cl cannot easily displace I in $CsSnI_3$ perovskite, due to the size mismatch of the two halides, and so $SnCl_2$ is pushed to the surface of the crystallites, whilst still ensuring that the perovskite is formed in a tin-rich environment.; (ii) $SnCl_2$ is much more soluble in common solvents, including DMF, than SnF_2 due to its greater covalency, which is particularly important when processing films from solution at room temperature, as in our fabrication method.; (iii)The propensity for solid-state diffusion of tin chloride into fullerene is likely to be larger due to the smaller size and lower mass of chloride species compared to the iodide and bromide analogues.

In summary, a strategy for fabricating $CsSnI_3$ based photovoltaic devices with the highest fill factor reported for a tin PPV has been described, that simultaneously removes the requirement for an electron blocking layer at the hole-extracting electrode and the need for an additional processing step to minimise the density of pinholes in the perovskite film. We have shown that the improved performance and tolerance to pin-holes in the perovskite film stems from *n*-doping of the fullerene electron-transport layer by $SnCl_2$, and that the stability of unencapsulated $CsSnI_3$ devices based on a simplified EBL free device architecture is improved by at least an order of magnitude as compared to lead based PPV with the same architecture when tested under continuous simulated solar illumination in ambient air at 50°C. Taken together, the findings reported herein justify an intensive research effort into tin perovskite PVs, focused on improving η to a level comparable to that of lead perovskite PVs.

Methods

Materials

CsI (Sigma-Aldrich 99.9%), SnI_2 (Alfa Aesar, 99.999%), $SnCl_2$ (Sigma Aldrich, 99.99%), SnF_2 (Acros Organics, 99%), $SnBr_2$ (Alfa Aesar, 99.4%), Perovskite Precursor Ink (for nitrogen processing) (Ossila, 1:1:4 $PbCl_2$:PbI_2:CH_3NH_3I, 99.999%:99.999%:99%, 99.8% DMF), $PC_{61}BM$ (Solenne, 99.5%), bathocuproine (BCP) (Alfa Aesar, 98%), *N,N*-dimethylformamide (DMF) (VWR, anhydrous, 99.8%), chlorobenzene (Sigma-Aldrich, anhydrous, 99.8%), acetone (Sigma-Aldrich, GPR, 99%), propan-2-ol (Sigma-Aldrich, HPLC, 99.8%), deionised H_2O (purite dispenser, >10 MΩ). CsI and non-anhydrous solvents were stored in air. All other chemicals were stored in a nitrogen filled glove box (<5 ppm O_2 and <1 ppm H_2O).

B-γ $CsSnI_3$ films

In a dry nitrogen filled glovebox CsI, SnI_2 and tin(II) halide were mixed together in 1:1:0.1 molar ratio. To this mixture *N,N*-dimethylformamide (DMF) was added to make an 8 wt.% solution (total mass of solids), which was stirred overnight before use. To deposit films, two drops of solution were cast onto a substrate spinning at 4000 rpm for 60 seconds. The B-γ phase forms immediately upon solvent evaporation.

Device fabrication

Indium tin oxide (ITO) coated glass slides (Thin Films Devices Inc. 15 ± 3 Ω/sq.) were held in vertical slide holders and ultra-sonically agitated in an acetone bath, followed by a high purity water bath with a few drops of surfactant, followed by high purity deionized water only bath, and finally an isopropanol bath. After this, the slides were suspended in hot acetone vapour for 10 seconds before UV/O_3 treatment for 15 minutes.

Immediately after UV/O_3 treatment the slides were transferred into a dry nitrogen filled glovebox for $CsSnI_3$ film deposition, followed by deposition of a $PC_{61}BM$ film from 15 mg/ml chlorobenzene solution using a spin speed of 1500 rpm. The substrates were then loaded into a high vacuum thermal evaporator located in the same glovebox and 6 nm of bathocuproine (BCP) was deposited followed by 50 nm of Al at a pressure of 1×10^{-5} mbar (with substrate rotation). The Al electrode was deposited through a shadow mask to make six devices per slide, each with an area of 6 mm^2.

Device Testing

Device testing was performed in the same glove box as used for device fabrication or, as for the stability testing, using a solar simulator outside the glove box. Current density–voltage (*JV*) curves were measured using a Keithley 2400 source-meter under AM1.5G solar illumination at 100 mW/cm^2 (1 sun), scanned from −1 V to +1 V at 0.1 V/s. Devices exhibited no significant hysteresis (Figure S6). External quantum efficiency (EQE) measurements were carried out using a Sciencetech SF150 xenon arc lamp and a PTI monochromator, with the monochromatic light intensity calibrated using a Si photodiode (Newport 818-UV). The incoming monochromatic light was chopped at 180 Hz. For signal measurement a Stanford Research Systems SR 830 lock-in amplifier was used.

X-ray Diffraction (XRD)

XRD was performed on thin films of $CsSnI_3$ prepared from 16 wt.% (total solids) DMF solution deposited onto a substrate spinning at 4000 rpm for 60 seconds. A thicker film than used in the devices was used here to obtain sufficient signal for the time dependent studies. Scans were recorded under a flow of gas (dry nitrogen, dry air, humid nitrogen or ambient air) using a Cu $K\alpha_{1/2}$ source in θ-θ mode on a Bruker D8 Advance powder diffractometer equipped with an Anton-Paar HTK900 gas chamber. Humid nitrogen was introduced by bubbling through water before the chamber. The measured XRD patterns were corrected for height offset (due to the thickness of the film) by calibrating the 2θ scale with reference the expected peak positions for pure B-γ $CsSnI_3$. Simulated diffraction patterns were calculated using the program Mercury 3.1 using CIFs from the Inorganic Crystal Structure Database (ICSD).

X-ray / Ultraviolet Photoelectron Spectroscopy

XPS was performed on film on gold coated glass substrates using a Kratos AXIS Ultra DLD. Samples were unavoidably exposed to air for approximately 1 minute during transfer from an air tight box to the vacuum chamber of the instrument. XPS measurements were carried out in a UHV system with a base pressure of 5×10^{-11} mbar. The sample was excited with X-rays from a mono-chromated Al $K\alpha$ source ($h\nu$ = 1486.7 eV) with the photoelectrons being detected at a 90° take-off angle. The sputtering was carried out at room temperature using a Minibeam I ion gun (Kratos Analytical, UK). A beam of 4 keV Ar^+ ions were incident on a 3 $\times$ 3 mm area of the sample surface. Curve fitting was performed using the CasaXPS package, incorporating Voigt (mixed Gaussian-Lorentzian) line shapes and a Shirley background.

UPS was performed in the same vacuum system as for XPS using a He 1 α source at 21.22 eV.

Electronic Absorption Spectroscopy

UV/Vis/NIR spectra were measured for optically thin films of $CsSnI_3$ on glass or ITO substrates. Experiments from the same set were performed on the same day.

Contact potential measurement

Work function measurements were performed using a Kelvin probe referenced to freshly cleaved highly oriented pyrolytic graphite in a nitrogen-filled glove box co-located with the spin coater and thermal evaporator.

References

1. Kojima, A., Teshima, K., Shirai, Y. & Miyasaka, T. Organometal halide perovskites as visible-light sensitizers for photovoltaic cells. *J. Am. Chem. Soc.* **131,** 6050–6051 (2009).

2. NREL chart. Accessed 06/05/2016 (2016). Available at: http://www.nrel.gov/ncpv/images/efficiency_chart.jpg.

3. Pyykkö, P. Relativistic effects in structural chemistry. *Chem. Rev.* **88,** 563–594 (1988).

4. Boix, P. P., Agarwala, S., Koh, T. M., Mathews, N. & Mhaisalkar, S. G. Perovskite Solar Cells: Beyond Methylammonium Lead Iodide. *J. Phys. Chem. Lett.* **6,** 898–907 (2015).

5. Noel, N. K. *et al.* Lead-Free Organic-Inorganic Tin Halide Perovskites for Photovoltaic Applications. *Energy Environ. Sci.* **7,** 3061–3068 (2014).

6. Hao, F., Stoumpos, C. C., Cao, D. H., Chang, R. P. H. & Kanatzidis, M. G. Lead-free solid-state organic–inorganic halide perovskite solar cells. *Nat. Photonics* **8,** 489–494 (2014).

7. Xu, P., Chen, S., Xiang, H.-J., Gong, X.-G. & Wei, S.-H. Influence of Defects and Synthesis Conditions on the Photovoltaic Performance of Perovskite Semiconductor $CsSnI_3$. *Chem. Mater.* **26,** 6068–6072 (2014).

8. Kumar, M. H. *et al.* Lead-Free Halide Perovskite Solar Cells with High Photocurrents Realized Through Vacancy Modulation. *Adv. Mater.* **26,** 7122–7127 (2014).

9. Yokoyama, T. *et al.* Overcoming Short-Circuit in Lead-Free $CH_3NH_3SnI_3$ Perovskite Solar Cells via Kinetically Controlled Gas–Solid Reaction Film Fabrication Process. *J. Phys. Chem. Lett.* **7,** 776–782 (2016).

10. Shockley, W. & Queisser, H. J. Detailed Balance Limit of Efficiency of p-n Junction Solar Cells. *J. Appl. Phys.* **32,** 510–519 (1961).

11. Chung, I. *et al.* $CsSnI_3$: Semiconductor or metal? High electrical conductivity and strong near-infrared photoluminescence from a single material. High hole mobility and phase-transitions. *J. Am. Chem. Soc.* **134,** 8579–8587 (2012).

12. Huang, L. & Lambrecht, W. R. L. Electronic band structure, phonons, and exciton binding energies of halide perovskites $CsSnCl_3$, $CsSnBr_3$, and $CsSnI_3$. *Phys. Rev. B* **88,** 165203 (2013).

13. Chen, Z. *et al.* Photoluminescence study of polycrystalline $CsSnI_3$ thin films: Determination of exciton binding energy. *J. Lumin.* **132,** 345–349 (2012).

14. Zhang, J. *et al.* Energy barrier at the N719-dye/$CsSnI_3$ interface for photogenerated holes in dye-sensitized solar cells. *Sci. Rep.* **4,** 6954 (2014).

15. Stoumpos, C. C., Malliakas, C. D. & Kanatzidis, M. G. Semiconducting tin and lead

iodide perovskites with organic cations: phase transitions, high mobilities, and near-infrared photoluminescent properties. *Inorg. Chem.* **52,** 9019–9038 (2013).

16. Hao, F. *et al.* Solvent-Mediated Crystallization of $CH_3NH_3SnI_3$ Films for Heterojunction Depleted Perovskite Solar Cells. *J. Am. Chem. Soc.* **137,** 11445–11452 (2015).

17. Sabba, D. *et al.* Impact of Anionic Br- Substitution on Open Circuit Voltage in Lead Free Perovskite ($CsSnI_{3-x}Br_x$) Solar Cells . *J. Phys. Chem. C* **119,** 1763–1767 (2015).

18. Chen, Z., Wang, J. J., Ren, Y., Yu, C. & Shum, K. Schottky solar cells based on $CsSnI_3$ thin-films. *Appl. Phys. Lett.* **101,** 93901 (2012).

19. Marshall, K. P., Walton, R. I. & Hatton, R. A. Tin Perovskite / Fullerene Planar Layer Photovoltaics: Improving the Efficiency and Stability of Lead-Free Devices. *J. Mater. Chem. A* **3,** 11631–11640 (2015).

20. Koh, T. M. *et al.* Formamidinium tin-based perovskite with low E_g for photovoltaic applications. *J. Mater. Chem. A* **3,** 14996–15000 (2015).

21. Zhang, M. *et al.* Low-temperature processed solar cells with formamidinium tin halide perovskite/fullerene heterojunctions. *Nano Res.* **9,** 1570–1577 (2016).

22. Werker, W. Die Kristallstruktur des Rb_2SnI_6 und Cs_2SnI_6. *Recl. des Trav. Chim. des Pays-Bas* **58,** 257–258 (1939).

23. Lee, B. *et al.* Air-Stable Molecular Semiconducting Iodosalts for Solar Cell Applications: Cs_2SnI_6 as a Hole Conductor. *J. Am. Chem. Soc.* **136,** 15379–15385 (2014).

24. Xiao, Z., Zhou, Y., Hosono, H. & Kamiya, T. Intrinsic defects in a photovoltaic perovskite variant Cs_2SnI_6. *Phys. Chem. Chem. Phys.* **17,** 18900–18903 (2015).

25. Peedikakkandy, L. & Bhargava, P. Composition Dependent Optical, Structural and Photoluminescence Characteristics of Cesium Tin Halide Perovskites. *RSC Adv.* **6,**

19857–19860 (2016).

26. Shannon, R. D. Revised Effective ionic radii and systematic studies of interatomic distances in halides and chalcogenides. *Acta Crystallogr. Sect. A Found. Adv.* **A32,** 751–767 (1976).

27. Moses, P. R. *et al.* X-ray Photoelectron Spectroscopy of Alkylamine-Silanes. *Anal. Chem.* **50,** 576–585 (1978).

28. Alonzo, G. *et al.* Mössbauer, Far-Infrared, and XPS Investigations of SnCl2 and SnCl4 Introduced in Polyconjugated Monosubstituted Acetylene Matrices. *Appl. Spectrosc.* **49,** 237–240 (1995).

29. Zhang, Y. *et al.* Flexible, hole transporting layer-free and stable $CH_3NH_3PbI_3$/ $PC_{61}BM$ planar heterojunction perovskite solar cells. *Org. Electron.* **30,** 281–288 (2016).

30. Chung, I., Lee, B., He, J., Chang, R. P. H. & Kanatzidis, M. G. All-solid-state dye-sensitized solar cells with high efficiency. *Nature* **485,** 486–489 (2012).

31. Tyler, M. S., Nadeem, I. M. & Hatton, R. A. An electrode design rule for high performance top-illuminated organic photovoltaics. *Mater. Horiz.* **3,** 348–354 (2016).

32. Yan, Y. Perovskite solar cells: High voltage from ordered fullerenes. *Nat. Energy* **1,** 15007 (2016).

33. Shao, Y., Yuan, Y. & Huang, J. Correlation of energy disorder and open-circuit voltage in hybrid perovskite solar cells. *Nat. Energy* **1,** 15001 (2016).

34. Saparov, B. *et al.* Thin-film deposition and characterization of a Sn-deficient perovskite derivative Cs_2SnI_6. *Chem. Mater.* **28,** 2315–2322 (2016).

35. Glen, T. S. *et al.* Dependence on Material Choice of Degradation of Organic Solar Cells Following Exposure to Humid Air. *J. Polym. Sci. Part B Polym. Phys.* **54,** 216–224 (2016).

Acknowledgements

The authors would like to thank the United Kingdom Engineering and Physical Sciences Research Council (EPSRC) for funding (Grant numbers: EP/L505110/1 & EP/N009096/1). All data supporting this study are provided as supplementary information accompanying this paper.

Author contributions

KPM performed all of the experimental work. KPM, RIW and RAH conceived the experiments, analysed the results and wrote the paper. MW collected the XPS and UPS data and helped to analyse the results.